Abstract

Electrochemical oxidation of urea provides an approach to prevent excess urea emissions into the environment while generating value by capturing chemical energy from waste. Unfortunately, the source of high catalytic activity in state-of-the-art doped nickel catalysts for urea oxidation reaction (UOR) activity remains poorly understood, hindering the rational design of new catalyst materials. In particular, the exact role of cobalt as a dopant in $Ni(OH)_2$ to maximize the intrinsic activity towards UOR remains unclear. In this work, we demonstrate how tuning the Ni:Co ratio allows us to control the intrinsic activity and number of active surface sites, both of which contribute towards increasing UOR performance. We show how $Ni_{90}Co_{10}(OH)_2$ achieves the largest geometric current density due to the increase of available surface sites and that intrinsic activity towards UOR is maximised with $Ni_{20}Co_{80}(OH)_2$. Through density functional theory calculations, we show that the introduction of Co alters the Ni 3d electronic state density distribution to lower the minimum energy required to oxidize Ni and influence potential surface adsorbate interactions.

Keywords

urea oxidation reaction; electronic structure; nickel-cobalt hydroxide; electrocatalysis; DFT; sol-gel

Introduction

Wastewater enriched with urea is an abundant and untapped source of energy generated by industrial urea fertilizer production and human metabolic processes.[1] If untreated before release into the environment, urea will decompose into toxic nitrogen oxides and cyanate salts, both of which are harmful to humans and aquatic ecosystems.[2,3] Traditional wastewater treatment methods to remove urea such as

high pressure-temperature hydrolysis, biological decomposition, and decomposition by strong oxidants, provide sustainable solutions for closing nitrogen cycle, but fail to extract value from this energy-rich compound.[4] Electrochemical oxidation of urea is an attractive candidate to replace current urea-removal methods as it enables the capture of the chemical energy stored in the bonds of urea, and is facilitated by inexpensive catalyst materials.[5–8] In this regard, UOR continues to attract considerable attention as an alternative to direct water oxidation as an anodic reaction in the electrochemical generation of hydrogen and CO_2 electrolysis to value-added products because of the lower voltage required to drive the reaction as well as the aforementioned abundance of environment-polluting urea available in wastewater streams.[9–11] Thus far, Ni(*II-IV*)-based materials such as oxides, hydroxides, sulfides, and others have shown the best catalytic performance towards UOR compared to other catalysts due to the *in-situ* generation of reactive nickel sites that act as oxidants towards urea.[11,12] However, the activity of these materials is known to become sluggish over time due the generation of carbonate at the surface over the course of a reaction.[13–15] To reduce changes in the surface and further improve the intrinsic activity of the catalyst towards UOR, researchers have begun to investigate the performance of binary and ternary multimetal electrocatalysts.[5–8]

Among the binary transition metal catalysts studied for UOR, mixtures of Ni and Co with non-zero valences have attracted attention due to their increased current densities, reduced onset potentials, and prolonged stability relative to other Ni(*II-IV*)-based systems mixed with a secondary metal.[5,8,16,17] While the optimal composition in $Ni_{1-x}Co_x(OH)_2$ catalysts is reported as $Ni_{90}Co_{10}(OH)_2$ or $Ni_{80}Co_{20}(OH)_2$ depending on compositions studied, the nature of the enhancement and the cause for its maximization between 10-20% Co incorporation still remains unclear (see table S2 in SI for a literature summary of $Ni_{1-x}Co_x(OH)_2$ based catalysts for UOR). Several studies have concluded that changes in electrical conductivity due to Co incorporation or increases in the electrochemically active surface area are not the origin of enhanced UOR.[18–20] In addition, it is known that adding Co can increase the number of Ni(*IV*) surface sites (postulated

to be the most active toward UOR).[11,21,22] The number of Ni(*IV*) sites is expected to be maximized with a Co incorporation for either $Ni_{60}Co_{40}(OH)_2$ or $Ni_{50}Co_{50}(OH)_2$, which conflicts with the trend discussed above for the best performing $Ni_{1-x}Co_x(OH)_2$ UOR catalyst.[17,18,21,22] Thus, the origin of UOR enhancement is thought to be caused by Co-induced changes to the electronic structure of Ni however, more in-depth studies are needed to verify this.[23–25]

Herein we explore the effect of Co incorporation on Ni UOR activity and investigate Co-induced changes to Ni electronic structure by combining electrochemical analysis and density functional theory (DFT) calculations. The prepared catalysts were characterized by energy dispersive X-ray spectroscopy (EDX), powder X-ray diffraction (PXRD), and UV-Vis spectroscopy. Through electrochemical screening of each composition by cyclic voltammetry (CV) we observed that the number of available surface sites and their intrinsic activity can be tuned by altering the Co fraction in $Ni_{1-x}Co_x(OH)_2$. The influence of electronic structure of neighboring Co atoms on the electronic structure of Ni in $Ni(OH)_2$ surface doped with Co was elucidated by DFT, allowing us to draw conclusions about enhanced UOR activity.

Experimental Methods

Synthesis of Materials

Synthesis of $Ni_{1-x}Co_x(OH)_{2-y}Cl_y$. The synthesis of $Ni_{1-x}Co_x(OH)_{2-y}Cl_y$ was adapted from elsewhere with modifications to improve reaction mixing and temperature control.[11,26] To begin, a total of 0.9 mmol of Ni(*II*)Cl_2•$6H_2O$ (Sigma; 99.9% trace metals basis) and Co(*II*)Cl_2•$6H_2O$ (Sigma; 98% ACS Grade) was added to centrifuge tubes and dissolved in 4.0 mL absolute ethanol (>99.9% ACS grade). The tubes were then sonicated for < 10 s to ensure a homogenous distribution of metal ions was achieved followed by the fast addition of 1.4 mL of propylene oxide (Sigma; ≥99.5% GC basis) (PO). Immediately after PO addition, the

tubes were capped and sealed with parafilm, then shaken using an Eppendorf Thermomixer C at 30°C at 450 RPM for 24 hours. Afterwards, each tube was filled with ~11 mL anhydrous acetone (Sigma; ≥99.9 HPLC Grade), then decanted to remove the supernatant which contained the majority of unreacted precursors. The tubes were then filled with anhydrous acetone and allowed to sit for 24 hours to undergo solvent exchange from the pores of the gel. After 24 hours, the supernatant was decanted and replaced; this process was repeated three more times for a total of five solvent exchange cycles. After the final solvent exchange, the tubes were decanted and dried using a rotary evaporator at 30°C under a vacuum of ~730 mm Hg for 8 hours to form a xerogel. The xerogels were then ground into a powder and placed under vacuum at 25°C for 60 hours to remove residual solvent.

Physical Characterization

ICP-MS measurements. Powdered catalysts (29-30 mg) were digested in 20 mL 2% HNO_3 for 72 hours in glass scintillation vials. Two successive 10x dilutions were then performed to get a final total Co+Ni concentration of approximately 100 ppm. Samples were submitted to the Metal Isotope Geochemistry Laboratory in the Earth Science department at the University of Waterloo. Class A volumetric glassware was used for preparing solutions used in this analysis. A 200 µL autopipette was calibrated and used for diluting the digestate. All glassware and pipette tips were soaked in 2% HNO_3 prior to rinsing with MilliQ water before use.

SEM-EDX sample measurements. Catalyst inks were made by mixing 2 mg of catalyst material with 1 mg Vulcan Carbon Black (FuelCellStore), 400 µL absolute ethanol (>99.9% ACS grade) and 100 µL MilliQ water (18.2 Ω). Ink mixtures were sonicated for 1 hour after which the catalyst ink was drop cast onto Toray 60 Carbon paper (FuelCellStore); the volume of ink deposited was adjusted to get 0.226 mg cm^{-2} on each

sample. EDX analysis including elemental and phase mapping was performed on an FEI Quanta FEG 250 environmental scanning electron microscope.

SEM and TEM imaging. For high magnification imaging, catalyst inks were made by mixing catalysts with MilliQ water (18.2 Ω) in a 4:3 mg : mL ratio and sonicated for 10 minutes. Ink droplets were dropcast onto Cu/C TEM grids and imaged on a Hitachi HF3300 microscope. Low magnification imaging was performed using an FEI Quanta FEG 250 environmental scanning electron microscope.

PXRD sample preparation. PXRD measurements were conducted at room temperature on a PANalytical Empyrean diffractometer with Cu-Kα radiation equipped with a PIXcel bidimensional detector. Powdered samples were measured on zero-background substrate using a Bragg-Brentano geometry. Phase pattern simulations were done by modifying the c axis of CIF files (β-$Ni(OH)_2$: ICSD-161894, β-$Co(OH)_2$: ICSD-26763) to match the experimental interlamellar spacing. The modified CIF files used in the complete integration method in real space (CIREALS) method described elsewhere reproduced the experimental peak positions and relative order of intensity for both pure Ni and Co phases.[27]

UV-Vis measurements. The absorbance spectra of powdered catalyst samples were measured by reflectance UV-Vis using a R200-Angle Ocean Optics Reflection probe at a distance of ~3 cm with a deuterium-halogen light source (DH-2000-BAL) and Ocean Optics Flame Miniature Spectrometer. The background reflectance spectrum for all measurements was taken from a polished slab of PTFE.

Raman Spectroscopy measurements. Raman spectroscopy was conducted with a Renishaw inVia Raman microscope. All spectra were acquired using a 532 nm laser filtered to 10% laser power with neutral density filters. Each spectrum had an acquisition time of 300 seconds, except 100% Co which required 150 seconds due to laser damage. Spectra were analyzed in Renishaw WiRE V5.3 software to perform polynomial baseline subtractions and curve fitting.

X-ray photoelectron measurements. X-ray photoelectron spectroscopy was performed using the ThermoFisher Scientific K-Alpha X-ray photoelectron spectrometer. Samples were prepared by activating anodes as described below, followed by immediately rinsing with MilliQ water and drying under a stream of Ar. The as-prepared samples were stored under Ar prior to the analysis**.**

Electrochemical Assessment

Anode Preparation. Catalyst inks were made by mixing 2 mg of catalyst material with 1 mg Vulcan Carbon Black (FuelCellStore) then adding 390 µL absolute ethanol (>99.9% ACS grade) and 100 µL MilliQ water (18.2Ω). The mixture was sonicated briefly (<3 s) to disperse the powder in the solvent before the addition of 10 µL of Nafion D-520 dispersion (Alfa Aesar; 42118). Ink mixtures were sonicated for 1 hour, after which five layers of catalyst ink were dropcast onto a 0.58±0.04 cm^2 piece of Toray 60 Carbon paper (FuelCellStore) such that the total volume of ink deposited was adjusted to get 0.226 mg cm^{-2} on each anode.

Evaluation of UOR activity. Evaluation of UOR activity was performed in 1M aqueous KOH (Sigma; ≥85% ACS Grade) electrolyte containing 0.33 M urea (Sigma; ≥99.5% ReagentPlus) in deionized water (18.2Ω). The electrolyte was purged with Ar prior to use. All electrochemical measurements took place in an undivided three-electrode cell with a double junction Ag/AgCl (3.5M KCl) reference electrode and Pt mesh counter electrode. Catalysts were first activated in 50 mL 1M KOH by CV cycles scanning from -0.4 to 0.8 V vs Ag/AgCl at 100 mV/s for 50 scans using a potentiostat (Biologic SP-300). This was followed by CV cycles within the same range at 20 mV/s for 20 scans to achieve a steady state. CV was used to assess the activity differences between activated catalysts with different Ni:Co ratios in 50 mL 1M KOH and 50 mL 1M KOH + 0.33M urea by scanning from -0.4 to 0.8 V vs Ag/AgCl at 20 mV/s for 10 scans. Potentials were

converted to V vs RHE using equation 1 below and assuming that the bulk pH was the same as the local pH at the electrode.

$$E_{RHE} = E_{Ag/AgCl,3.5M\ KCl} + 0.059\ pH + E^{\circ}_{Ag/AgCl,3.5M\ KCl} \quad (1)$$

Current densities were normalized by both the geometric surface area of the catalyst film and the number of redox active surface sites (RASS). The RASS was determined by performing a linear integration of a baseline subtracted current in the redox active region. The Butler-Volmer equation was first used to fit the raw current data between 1.23-1.64 V vs RHE to subtract the theoretical OER current from the redox-active region.[28] The capacitance current (from 0.8-1.23 V vs RHE) and remaining OER current (1.64-1.831 V vs RHE) were then fit to polynomials to construct a baseline. Each baseline was then subtracted from the raw current in the corresponding potential region. All baselines for each composition with subtracted current data are shown in the SI. To convert the charge from the integrated redox region into the number of RASS, we assumed that the entire region was associated with a 1e- transfer process, as reported recently in work by *Anantharaj et al.*[29] Since, we observed a redox peak for Co(*III*) to Co(*IV*), we validated this assumption by examining how the number of active surface sites would scale by approximating the total number of electrons for the sum of both processes in the redox region based on the ratio of Ni:Co (see SI for details). It should be noted that this assumption overestimates the total number of electrons at low Co levels since the literature suggests that Co in $Ni(OH)_2$ is redox inactive at low concentrations.[22]

Theoretical Methods

PDOS and Charge Density Difference Calculations. Density Functional Theory (DFT) calculations were conducted using the Vienna Ab-initio Simulation Package (VASP) within the Python-based Atomic Simulation Environment (ASE).[30–34] To account for the self-repulsion of elections in the d-orbitals that has been previously reported to result in spurious occupation and bandgap prediction, the generalized gradient approximation with Hubbard correction potential (GGA+U) method was used with the BEEF-vdW

158 exchange-correlation functional.[35–37] Spin-polarization calculations were carried out in the
159 antiferromagnetic configuration with initialized magnetic moments of 1.6 μB and 2.2 μB for Ni and Co
160 atoms, respectively, which allowed us to get final magnetic moments similar to experimental values (See
161 Figures S29-33). The β-$Ni(OH)_2$ bulk unit cell (mp-27912 primitive cell structure) was relaxed until the
162 atomic forces were minimized to be less than 0.05 eV/Å using an energy cut-off of 800 eV and sampled
163 with a Monkhorst-Pack k-point mesh of (16x16x8); this cell relaxation was carried out twice consecutively
164 to remove Pulay stress from the final optimized structure. The optimized bulk cell was then propagated
165 into a (2x2x4) supercell with a vacuum length of 15 Å between repeating layers in the *z* direction.
166 Interactions between periodic images were decoupled in the *z* direction with a dipole correction[38]. For
167 geometry optimizations, the bottom two layers of the supercell had their positions constrained and the
168 rest of the cell was relaxed with an energy cut-off of 500 eV and sampled with a with a Monkhorst-Pack
169 k-point mesh of (4x4x1). To calculate the projected density of states and the charge density difference,
170 the optimized (2x2x4) supercells first underwent a self-consistent calculation with an energy cut-off of
171 500 eV and sampled with a Monkhorst-Pack k-point mesh of (4x4x1), to get an approximation of the
172 starting wavefunctions and charge density for use in subsequent calculations. Following this, a non-self-
173 consistent calculation starting from the previous wavefunctions and charge densities sampled with a
174 Monkhorst-Pack k-point mesh of (9x9x1) was conducted. To obtain the projected density of states,
175 VASPKIT was used to parse the calculated data.[39] The charge density differences of Co doped surfaces
176 were generated in VESTA based on equation 2 below.[40]

177 $$\Delta\rho_{doped\ surface} = \rho_{doped\ supercell} - \rho_{isolated\ dopant\ atom(s)} +$$

178 $$\rho_{isolated\ Ni\ atom(s)\ in\ dopant\ site(s)} - \rho_{undoped\ supercell} \quad (2)$$

179

Determination of Hubbard Potentials. Due to the large variation of U potentials for Ni and Co oxides and oxyhydroxides, along with the lack of reported U potentials for Ni and Co in the β-$M(OH)_2$ lattice, we systematically determined the correct potentials by evaluating two of the most common methods: 1) linear response theory and 2) optimizing with different values of U and comparing results to known experimental parameters. When evaluating the results of linear response theory based on the script posted in the VASP manual, U=4.64eV for Ni in β-$Ni(OH)_2$.[41,42] We found that when used in self-consistent calculations, this value of U resulted in unrealistic bandgap and local Ni magnetic moments compared to the experimental literature (E_g=~3.0-3.5 eV; 2.0±0.2 μB)[43,44], indicating that the electronic states have not been fully corrected. In contrast, fitting to experimental parameters provided reasonable results at the cost of an increased number of computations. From the TDOS of a (2x2x2) slab and fitting to experimental bandgaps, we found that the optimal U parameters for Ni and Co were 5.5 and 3.72 eV, respectively.

Results and discussion

1: Catalyst characterization

Inspired by recent reports of high UOR activity catalysts and the known ability to achieve homogenous doping, we optimized the epoxide sol-gel synthesis to controllably produce $Ni_{1-x}Co_x(OH)_2$ catalysts with specific Ni:Co ratios.[11,26,45] In order to verify that the element distribution is uniform, select Ni:Co sol-gel catalysts were imaged by SEM with spatial EDX mapping. As is evident from Figure 1a and Figures S1-S5, the mixing of metal cations across the surface was homogeneous. In addition, Figure 1b shows that the experimentally determined atomic ratio of Ni:Co by both EDX and ICP-MS was in good agreement with the ratio of metal precursors used in synthesis (see Figures S1-S6 for additional EDX data). Selected area EDX spectra show that the Cl content rises with increasing Co incorporation, suggesting different stochiometric ratios between the pure Ni and Co phases. To better understand the atomic

structure of the Ni and Co phases and their evolution with changing Ni:Co ratio, we used a combination of powder X-ray diffraction (PXRD), UV-Vis Spectroscopy, Raman Spectroscopy, and X-ray photoelectron spectroscopy (XPS) to extract structural and electronic changes.

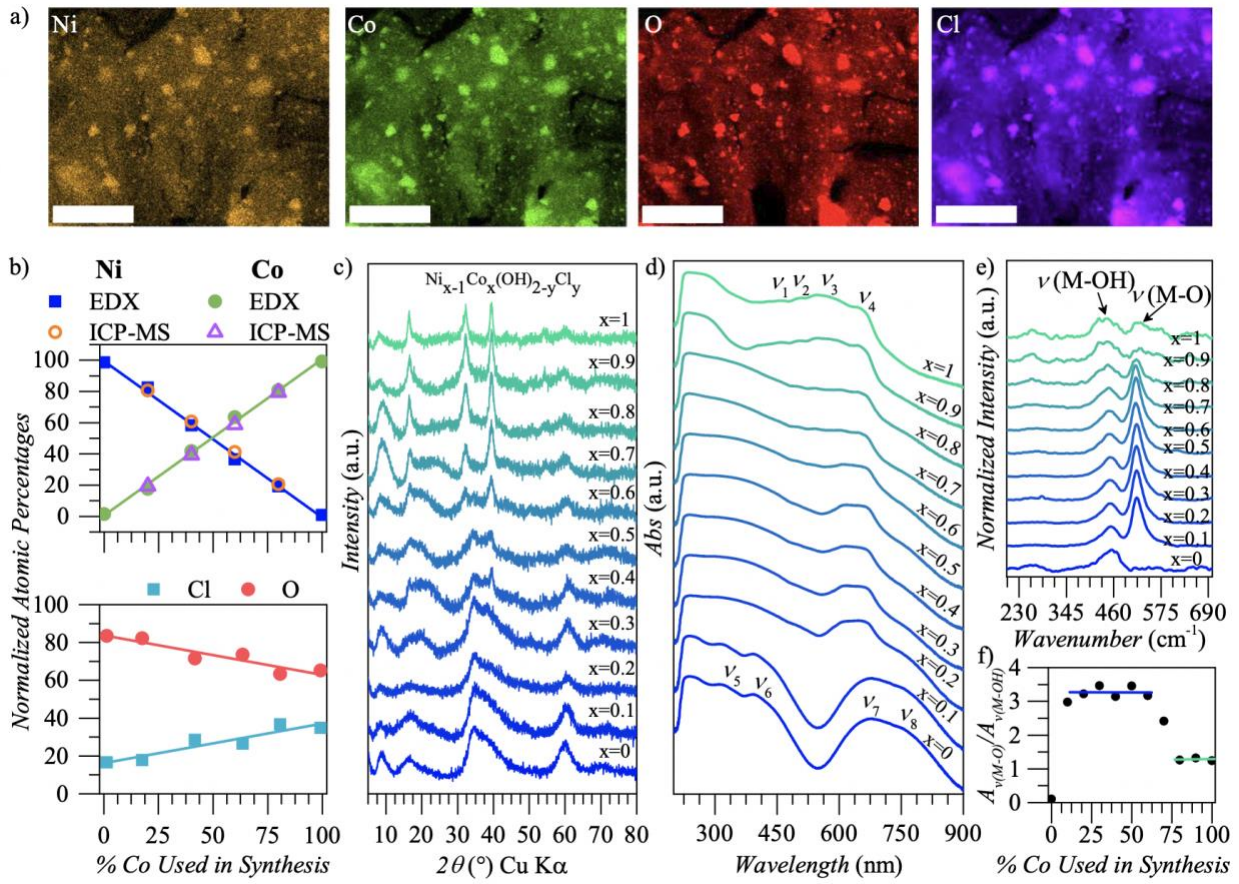

Figure 1: a) SEM-EDX spatial mapping of $Ni_{20}Co_{80}(OH)_2$ on carbon fiber paper. Scale bars are 20 µm. b) Change in atomic percentages of Ni, Co, Cl, and O measured by selected area EDX with additional ICP-MS characterization for Ni and Co. Ni-Co and Cl-O atomic percentages were normalized by either M/Ni+Co or X/Cl+O. c) PXRD of $Ni_{1-x}Co_x(OH)_2$ catalysts on a zero-background substrate. d) Normalized absorbance UV-Vis spectra of $Ni_{1-x}Co_x(OH)_2$ catalyst powders. e) Raman spectra of M-OH and M-O vibrations in $Ni_{1-x}Co_x(OH)_2$ catalysts. f) Raman spectroscopy correlation between υ(M-OH) and υ(M-O) peak areas from (f).

The PXRD patterns in Figure 1c show a gradual transition between the pure Ni phase (x=0) and pure Co phase (x=1), both of which appear to be the α- polymorphs of $Ni(OH)_2$ and $Co(OH)_2$ and match the results obtained from other Ni or Co epoxide sol-gel protocols, calculated PXRD patterns (see Figure S7 in the SI), and XRD patterns reported in the literature.[46–48] Qualitatively, the peak widths became narrower with increasing Co incorporation. This trend can be attributed to increased crystallinity of $Ni_{1-x}Co_x(OH)_2$ with increasing Co content, which was confirmed by high magnification transmission electron microscopy (TEM) imaging (Figure S9). While all studied compositions showed uniform surface coverage based on conventional scanning electron microscopy (SEM) analysis (Figure S10), high magnification TEM and SEM analysis revealed an increase in the number and size of observable crystallite domains and an associated change in nanoscale surface roughness. This trend in the morphology is in agreement with the commonly observed increase in the electrochemically active surface area (ECSA) and single crystal size in $Ni_{1-x}Co_x(OH)_2$ with increasing Co content.[19,20]

From the UV-Vis absorption spectra in Figure 1d, a gradual transition between the pure Ni and Co phases can be observed. In particular, the pure Ni phase in this work (x=0) has transitions assigned to Ni^{2+} in an octahedral environment (393 nm $^3T_{1g}(P)\leftarrow{}^3A_{2g}(F)$; 678 nm $^1E_g(G)\leftarrow{}^3A_{2g}(F)$ and a shoulder between 719-760 nm $^1E_g(D)\leftarrow{}^3A_{2g}(F)$) which have been previously reported for $Ni(OH)_2$ phases.[49,50] In addition to this, the transition at 310 nm suggests the presence of Ni^{3+} based on reports of a Ni(*III*) transition in Ni_2O_3 and Ni(*III*) complexes being in a similar range.[50,51] The $Co(OH)_2$ phase shows the presence of Co^{2+} transitions in octahedral (462 nm $^4T_{1g}(P)\leftarrow{}^4T_{1g}(F)$; 510 nm $^4A_{2g}(F)\leftarrow{}^4T_{1g}(F)$ and tetrahedral (546 nm $^4T_1(P)\leftarrow{}^4A_2(F)$; 641 nm $^4T_2(F)\leftarrow{}^4A_2(F)$) environments.[49,52–55] The presence of the tetrahedral Co environment in a layered hydroxide structure was previously demonstrated to occur in the presence of hydroxide substitution with chloride using both PXRD Rietveld refinements and X-ray absorption spectroscopy.[54] Based on these results, we hypothesize that the origin of the linear correlation between

Co and Cl concentrations observed in the elemental analysis is caused by the formation of tetrahedral Co sites in the lattice.

The calculated binding energies showed that the Ni 2p and Co 2p peaks are reduced with increasing fraction of Co incorporated in the catalyst (Figure S14). The change of binding energies for the Ni $2p_{1/2}$ and $2p_{3/2}$ states typically observed in XPS for Ni oxides and hydroxides was previously attributed to the nature of the ligand coordinated to Ni.[56] The reduction in binding energy is believed to originate from an increase of kinetic energy of the outgoing photoelectrons caused by the localization of unoccupied orbitals right above the Fermi level in a potential well.[56] In other words, the more unoccupied states become localized in the potential well, the larger the reduction in binding energy of the Ni 2p peaks we would expect to see. It is worth noting that the Co 2p peaks are moving towards the pure Co phase sample positions, while the Ni 2p peaks are moving below the pure Ni phase (Figure S14). This trend suggests that increasing the Co concentration increases the number of electrons that are localized at the Ni centers in these catalysts. During electrolysis, the valance states of catalysts of this type tend to increase, based on the reported *in situ* studies.[28,57,58]

Raman spectroscopy measurements (Figure 1e) show that the pure nickel hydroxide phase has a peak at 455 cm^{-1} wavenumbers which was assigned to the Ni-OH lattice vibration (υ(M-OH) in Figure 1e). Since this peak is in the range of reported experimental peak assignments for α- and β-$Ni(OH)_2$ vibrational modes (α- peaks 451-464 cm^{-1}; β-peaks 445-453 cm^{-1}), we cannot assign this peak to the Ni-OH lattice vibration from either of these two polymorphs.[48,59] The introduction of 10% Co led to the emergence of a new peak at 517 cm^{-1} (υ(M-O) in Figure 1e), which could originate from proton vacancies analogous to NiOOH regions within the bulk of the crystal lattice, as was previously reported for $Ni_{1-x}Co_x(OH)_2$ with Co concentrations as low as 1%.[60,61] The analysis of the ratio between the peak areas for υ(M-O) and υ(M-OH) modes (Figure 1f) revealed three regions across the composition range in these materials: 1) M-OOH rich region (blue line), 2) transition region (red line), and 3) M-OOH deficient region (green line). The

transition region correlates with the key changes in the PXRD patterns and UV-Vis spectra corelates and confirms the change in the number of M-OOH sites in the structure of $Ni_{x-1}Co_x(OH)_{2-y}Cl_y$.

2: Electrochemical measurements

The influence of Co on the electrochemical behaviour of the synthesized catalysts was probed by performing CV scans at 20 mV/s on activated materials (see experimental methods for the activation procedure) in 1 M KOH. Since UOR is reported to occur on oxidized $Ni(OH)_2$, we only show the anodic traces of all CV measurements in the main text (see Figure S16 for full CV scans). The electrochemical activation procedure performed prior to electrochemical characterization removed all Cl from the surface of the electrode as was confirmed by XPS analysis of the anodes before and after activation (Figure S15). Increasing the Co content in the catalyst material alters the position, width, and geometric current density (GCD) for the redox reactions associated with the oxidation of Ni and Co (Figure 2a).[12,57] The redox-active potential range increases with increasing Co incorporation along with a decrease in integrated area (Figure S18). From further analysis of the redox activity in KOH, we found that the Ni onset potential shifts towards lower potentials with increasing Co incorporation as predicted by the inductive effect (Figure 2e). In the context of this work, the inductive effect occurs by introducing a weaker Lewis acid than the parent metal, i.e. Co(*II*) in a Ni(*II*) matrix, which pushes electron density towards the parent metal and shifts the antibonding states toward the Fermi level, resulting in a decrease in the redox potential of Ni.[62] This decrease in redox potentials is well known to reduce the intrinsic oxygen evolution reaction (OER) activity of Ni surface sites. Hence, this evidence supports the notion that Co modulates the electronic states in $Ni(OH)_2$. Furthermore, it was suggested that Co shifts the electronic states of Ni by changing the energy of the O 2p states that bond with the Ni 3d states. This specific electronic state modulation route has not been explicitly demonstrated the $Ni_{1-x}Co_x(OH)_2$ system.

We note that Co is redox-active in a similar region as Ni and can potentially act as an active site for OER. In addition to Co having an inductive effect on neighbouring Ni sites, Ni could also have an inductive effect on the Co sites, shifting the Co redox potentials to more positive values, thereby making any attempt of deconvoluting the true Ni and Co redox peaks with confidence difficult. Hence, to normalize for the intrinsic activity we combined two classical electrochemistry approaches that were described recently in the context of doped $Ni(OH)_2$ materials.[28,29] First, baselines were constructed to capture the capacitance current and OER current by combining a polynomial fit with the Butler-Volmer equation such that, once subtracted from the raw current, the remainder only shows the faradaic current related to Ni and Co redox reactions (Figures 2b-c; see experimental for fitting details). The area under the redox-active region was then integrated with a linear baseline to extract the charge related to the oxidation of all redox-active sites. We then normalized the charge by the elementary charge of 1 electron to determine the redox active surface sites (RASS; discussed in detail in the SI). By examining the change in RASS before and after evaluating UOR activity we were able to evaluate the stability of materials as a function of Co incorporation (Figure S20; in the SI). This analysis showed that the addition of Co improves the stability but does not change significantly with increasing Co doping (see the SI for details).

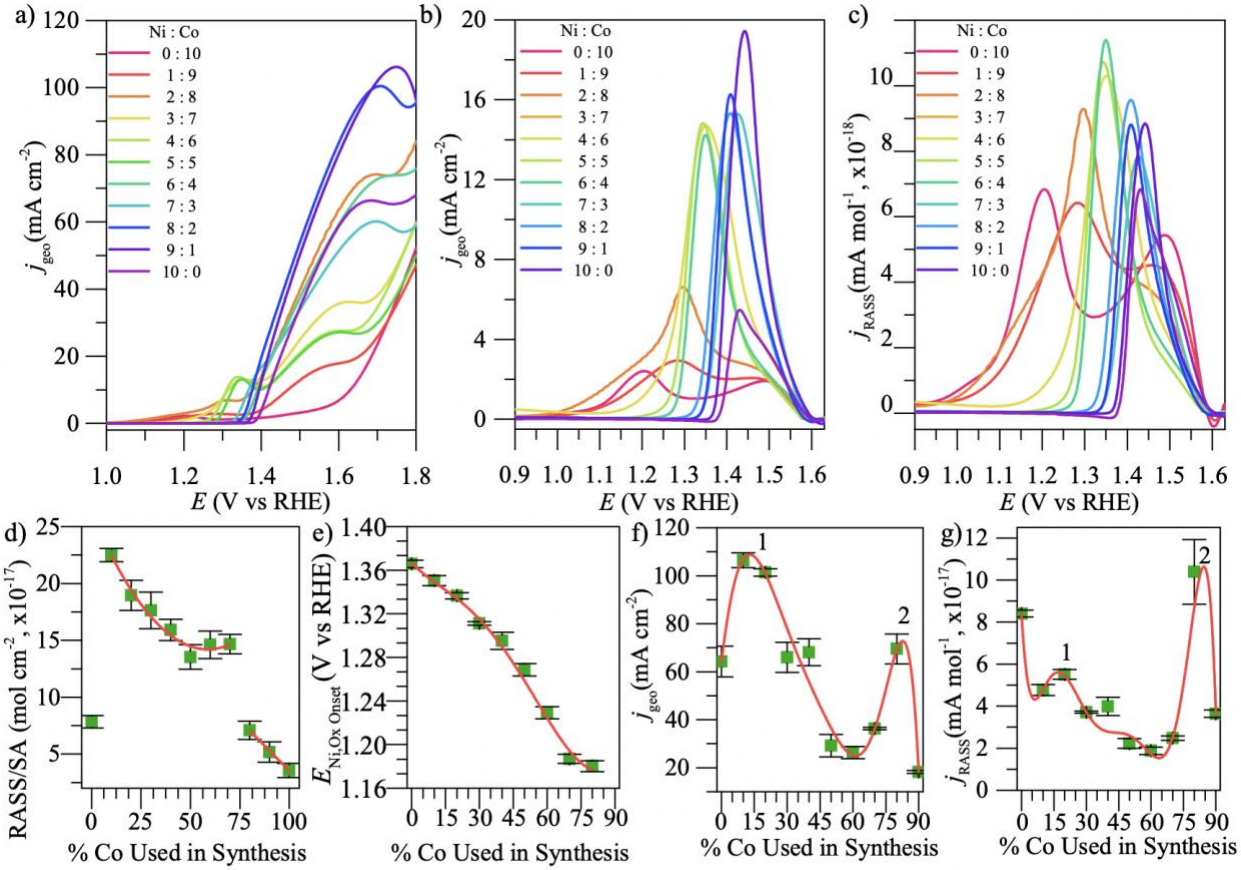

Figure 2: a) Anodic CV sweeps of activated $Ni_{1-x}Co_x(OH)_2$ catalysts in 1M KOH with 0.33M urea at 20 mV/s normalized by the geometric surface area. b) Anodic CV sweeps of activated $Ni_{1-x}Co_x(OH)_2$ catalysts in 1M KOH at 20 mV/s normalized by the geometric surface area with OER current subtracted. c) Anodic CV sweeps of activated $Ni_{1-x}Co_x(OH)_2$ catalysts in 1M KOH at 20 mV/s normalized by the number of RASS with OER current subtracted. d) Change in the number of RASS normalized by surface area with increasing Co concentration in $Ni_{1-x}Co_x(OH)_2$ catalysts. e) Change in Ni oxidation onset potential with increasing Co concentration in $Ni_{1-x}Co_x(OH)_2$ catalysts. f) Change in maximum GCD of UOR peak with increasing Co concentration in $Ni_{1-x}Co_x(OH)_2$ catalysts. g) Change in maximum current density per number of RASS of UOR peak with increasing Co concentration in $Ni_{1-x}Co_x(OH)_2$ catalysts.

With the normalized baseline and the OER-deconvoluted current in Figure 2c, the peak current per RASS is maximized at $Ni_{60}Co_{40}(OH)_2$ suggesting that the intrinsic activity towards oxidizing Ni is maximized here. When comparing how the number of RASS per geometric surface area change with composition (Figure 2f), we noticed that as the amount of Co increased, the number of RASS decreased in a semi-linear fashion until the inflection at $Ni_{40}Co_{60}(OH)_2$. The deviation from the qualitatively linear trend coincides with the appearance of $Co(OH)_2$ features in the PXRD (Figure 1c) and redox curves (Figure 2c), suggesting that this composition marks a transition point in both the structure and electrochemical behaviour towards increased $Co(OH)_2$ characteristics.

To understand the UOR performance of different activated $Ni_{1-x}Co_x(OH)_2$ catalysts, we performed CV as described in the experimental section. Figure 2a shows how the GCD differs as a function of Co composition in the catalyst. The highest current density was achieved with $Ni_{90}Co_{10}(OH)_2$, similar to what has been previously reported for $Ni_{1-x}Co_x(OH)_2$ hydroxide catalysts for UOR (see Table S1, S2, and S3).[17] Furthermore, we achieved a similar UOR response for the $Co(OH)_2$ phase as *Zhang et al.* which shows an increase in current in the presence of urea before the OER onset.[11] To analyse how the Co composition influenced UOR activity, the geometric and RASS-normalized peak current densities (Figures 2f-g) were plotted. In the GCD trend (Figure 2f), there are two clear peaks (denoted as 1 for $Ni_{80}Co_{20}(OH)_2$ and 2 for $Ni_{20}Co_{80}(OH)_2$ in the figure) that have larger GCDs than $Ni(OH)_2$, with a valley at $Ni_{40}Co_{60}(OH)_2$, the transition point mentioned above. Interestingly, when normalized by RASS (Figure 2g), peak 1 becomes smaller for pure $Ni(OH)_2$ while peak 2 relatively increases. This change in the trend suggests that peak 1 originates from maximizing the number of RASS participating in the reaction, while peak 2 is caused by maximization of the intrinsic activity of the catalyst towards UOR.

3: DFT calculations

In general, numerous reports indicate that changing the electronic structure of Ni is the most promising strategy for maximizing the intrinsic activity of UOR.[7] To investigate how Co will change the electronic states in the $Ni_{1-x}Co_x(OH)_2$ catalysts and subsequently deduce how this may influence intrinsic activity towards UOR, we performed DFT calculations for structures with increasing Co doping. It has been established that the degree of modification of the electronic structure depends on the way the dopant is incorporated into the catalyst and the concentration of the dopant.[45,63] While cation substitution can induce several forms of structural disorder in α- or β- polymorphs of $Ni(OH)_2$ (point defects, stacking faults, intercalation of foreign ions between layers, and different degrees of hydration, and α/β-interstratification to name a few), it is not necessary to model them to observe the effects Co atoms have on the electronic states in $Ni_{1-x}Co_x(OH)_2$ catalysts.[48] We chose to use $Ni(OH)_2$ as the base material in our model due to observations in this work and the literature that Co sites have very little activity towards UOR.[11,24] For both $Ni(OH)_2$ and $Co(OH)_2$, it is known that through both electrochemical activation and ageing in KOH electrolyte that intercalated ions (e.g. Cl^- in this work) and water are removed from between the layers, resulting in the material's transformation into the β- phase which is the most thermodynamically stable phase for both $Ni(OH)_2$ and $Co(OH)_2$.[11,64,65] Even though other different phases and materials such as α-$Ni(OH)_2$ and γ-NiOOH are known to form *in situ*, β-$Ni(OH)_2$ is likely the most dominant phase in our experiments due to chemical ageing prior to electrochemical testing. Thus, we modelled our system by studying the change in the electronic structure of β-$Ni(OH)_2$ with increasing concentration of Co in the top layer.

The initial magnetic moments in our models were set to be antiferromagnetic between neighbouring layers (along the *c* axis) based on neutron diffraction and magnetometer experiments reported in the literature.[43,44] To account for the self-repulsion of elections in the d-orbitals that have been previously reported to result in inaccurate occupancies and band gaps, the generalized gradient approximation with a Hubbard correction potential (GGA+U) method was used with the BEEF-vdW

354 exchange-correlation functional.[35–37] From an examination of the Hubbard potentials determined in the
355 literature, we noticed two key points. First, reports that determined U for Ni(*II*), did so for NiO or NiOOH
356 using the Perdew-Burke-Ernzerhof (PBE) functional (See Table S4 in the SI).[66] In addition, these reported
357 values vary between 4-7 eV depending on the method used.[67–70] Since it is not clear which value should
358 be used, we decided to first compare the two most commonly used methods to determine the Hubbard
359 potential in semiconductor materials to ensure that our calculation of the electronic state was accurate.

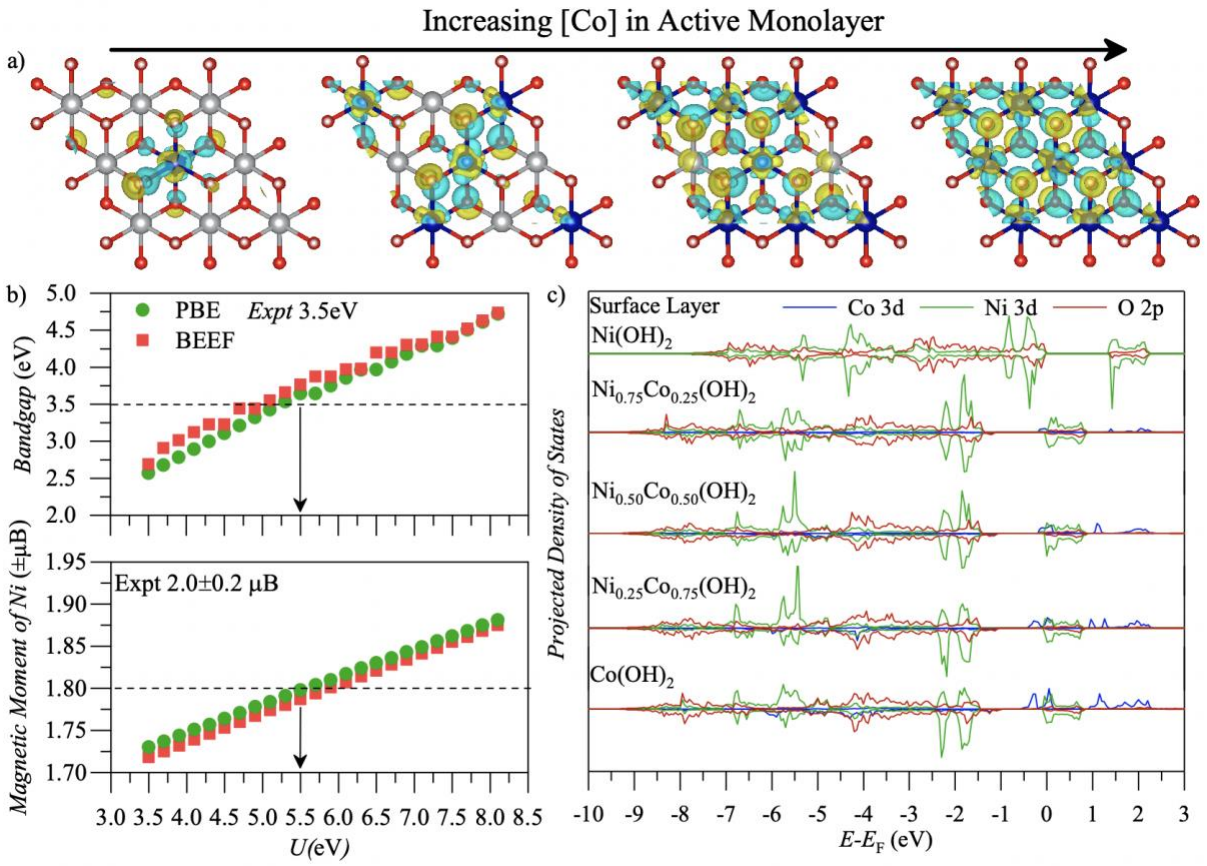

360

361 Figure 3: a) Charge density difference of Co doped surface from undoped surface. Yellow isosurfaces
362 represent electron density depletion, while blue isosurfaces represent electron density accumulation. The
363 sign of all charges used in calculations was positive. b) Changes in calculated bandgap and local magnetic
364 moments of Ni in bulk β-$Ni(OH)_2$ with different Hubbard potentials applied to Ni c) Projected density of

states showing the electronic state of 2x2x4 β-$Ni(OH)_2$ with increasing Co concentration in the surface layer of the supercell.

The first method is linear response theory, which is based on determining how the number of electrons at the atom of interest changes between self-consistent and non-self-consistent calculations over a range of Hubbard potentials.[41] A series of calculations were carried out over a range of U values (−0.20 to +0.20 V) for the bulk β-$Ni(OH)_2$ unit cell, resulting in a predicted Hubbard potential of 4.64 eV (see Figure S21 in the SI for calculation details).[42] Then, we conducted a series of calculations that consist of two-unit cell relaxations followed by one geometric relaxation (for calculation details, see SI). We then analyzed how the bandgap of the material from the density of states, and the local magnetic moment of Ni changed as a function of U. With this approach, an optical bandgap and the local magnetic moment of Ni that was similar to the experimental measurements for β-$Ni(OH)_2$ (E_g=~3.0-3.5 eV; 2.0±0.2 μB) was achieved with a Hubbard potential of 5.5 eV (Figure 3b).[43,44] It is worth noting that we also contrasted the difference between using PBE and BEEF functionals for these calculations and found that they both follow a nearly identical linear trend. Following these results, U for Co(*II*) in the bulk β-$Co(OH)_2$ unit cell was determined by matching the bandgap to the experimental value of 2.85 eV (see Figure S22 in the SI).[71] For Co, the value of U was found to be 3.72 eV, which is within the range of reported values of Co(*II*) in Co oxides (3-8 eV).[68,72–74] From these results, Hubbard potentials of 5.5 eV and 3.72 eV were used for Ni(*II*) and Co(*II*) for all remaining calculations in this work.

To understand how increasing the Co fraction in $Ni_{1-x}Co_x(OH)_2$ catalysts would alter the electronic structure, we first calculated the change in electron charge density from the pristine β-$Ni(OH)_2$ surface by doping the top monolayer in 25% increments, as shown in Figure 3a. Here, we can see that the charge density difference (CDD) surrounding the hydroxide moieties changes by decreasing the density along

with the Co-OH bond. The excess charge density is then distributed between the neighbouring Ni atoms bound to the perturbed hydroxide. This observation coincides with the experimental result that shows the redox potential continuously shifting towards more negative values based on the inductive effect described above. Furthermore, as the concentration of Co in the monolayer increases, we see that the charge accumulation becomes more aligned with the Ni-OH bond and that the charge density distribution surrounding the Ni atoms is perturbed.

While the observations in the CDD maps confirm the inductive effect occurs, we still lack an understanding of which electronic states are responsible for the observed changes. To address this, we performed projected density of states (PDOS) calculations using the same structural models used in the CDD calculations, as seen in Figure 3c. It appears that the addition of Co to the surface layer alters the Ni 3d states in several different ways. First, the anti-bonding states are shifted down monotonically as Co doping increased, which would alter the adsorption energy of different reaction intermediates in addition to oxidizing Ni. Hence, these results explain the experimental trends observed for the change in valence states for the Ni 2p and Co 2p measurements in Figure S14. Furthermore, we observed large changes in the Ni 3d density distribution with increases in Co concentration through an orbital decomposition of the projected density of states (see Figures S23-S27). Each decomposed projected state density will continuously shift downwards with increasing Co content of the surface layer, with the largest shift in energy occurring at the transition from 0 to 25% Co. The maximum population of each state was found to change when transitioning from 25 to 75% Co. In particular, the density of the majority spin of the $3d_{x^2-y^2}$ and $3d_{xy}$ states at -1.80 eV was reduced, while the state population maxima for the majority spin at -5 to -6 eV were gradually increased in density (Figures S24-25). The $3d_{z^2}$ state has a similar decrease in population for the majority spin at -1.80 eV, but a larger increase in the majority spin between -5 to -6 eV. Additionally, as the Co content in the surface layer increases there is an increase in the population of the minority spin at around -1.80 eV. The $3d_{xz}$ and $3d_{yz}$ orbital states, in contrast to the previously mentioned

Ni 3d-states have the smallest overall change in population density when increasing the amount of Co in the surface layer, which is likely caused by the low occupation of these states in pure β-$Ni(OH)_2$. Therefore, we can conclude that while all five Ni 3d states experience a similar downward shift in energy, the change in population density distribution altered by increasing the amount of Co atoms in the surface layer is most significant for the Ni $3d_{x^2-y^2}$,$3d_{xy}$, and $3d_{z^2}$ states. The surface Co composition ratios where the population densities are maximized (25% Co for the $3d_{x^2-y^2}$ and $3d_{xy}$ states and 75% Co for the $3d_{z^2}$ state) coincides with the experimental trends observed in this work for the change in electrochemical intrinsic activity towards UOR. This confirms that while the UOR activity on Co sites is very low compared to Ni sites, we can tune the electronic structure of Ni sites to maximize the intrinsic site activity of the anode towards UOR.

Conclusion

In summary, we demonstrated that changing the Co fraction in $Ni_{1-x}Co_x(OH)_2$ catalysts allowed us to tune the number of redox-active surface sites and the intrinsic activity of each site towards UOR. We found that the geometric current density for UOR was maximized for $Ni_{90}Co_{10}(OH)_2$ due to optimizing the number of redox-active surface sites that could participate in the reaction. Interestingly, the current density per number of redox-active sites was maximized for $Ni_{20}Co_{80}(OH)_2$, demonstrating an increase in intrinsic activity. To determine a theoretical explanation for the maximization of intrinsic activity at $Ni_{20}Co_{80}(OH)_2$, we performed density functional theory calculations to understand how the electronic structure of β-$Ni(OH)_2$ catalysts changes with increasing Co doping. We first systematically determined the correct Hubbard potentials for Ni and Co for our model to best predict the electronic properties of β-$Co(OH)_2$ and β-$Ni(OH)_2$. The charge density difference between undoped and surface doped (2x2x4) β-$Ni(OH)_2$ supercells were determined, showing that as we increase the Co fraction in the top layer more electron density is pushed towards the Ni atoms. Projected density of states calculations showed that

with increased Co incorporation in the surface layer the Ni 3d states experience a downward shift in energy and redistribution of orbital density. The projected density of states was then decomposed into each Ni 3d orbital, which demonstrated that while each state is lowered in energy with increased Co doping, unique features of the state density were enhanced for 25 and 75% Co incorporation in the surface layer. These results coincided with the two peaks in the experimentally observed intrinsic activity towards UOR for $Ni_{80}Co_{20}(OH)_2$ and $Ni_{20}Co_{80}(OH)_2$, revealing that multiple features in the Ni 3d electronic structure will have a significant influence over UOR performance. The altered Ni 3d states are likely related to changes in the adsorption and may stabilize certain reaction intermediates. To better understand how changes in the electronic structure affect specific intermediates, follow up studies should be focused on elucidating a detailed reaction mechanism both experimentally and theoretically on doped systems.

Acknowledgements

The authors thank Prof. Linda Nazar at the University of Waterloo for providing access to X-ray diffraction instrumentation, Prof. Rodney Smith at the University of Waterloo for performing Raman spectroscopy measurements, Prof. Brian Kendall and Sarah McCaugherty in the Metal Isotope Geochemistry Laboratory at the University of Waterloo for performing ICP-MS analysis, Peter Brodersen at the Ontario Center for the Characterization of Advanced Materials (OCCAM) for performing X-ray photoelectron spectroscopy analysis, Jason Tam and Mengsha Li at OCCAM for HR-STEM imaging, and Ilya Gourevich at the Centre for Nanostructure Imaging for performing SEM-EDX imaging. SWT thanks Dr. Jury J. Medvedev and Alexander W. H. Whittingham for helpful advice throughout the duration of this project. SWT, RMC and AK thank the University of Waterloo (Startup and Trailblazer Funding), Waterloo Institute for Nanotechnology (WIN-MESA+ Seed Funding), Natural Sciences and Engineering Research Council of Canada, Canadian Foundation for Innovation, and Ontario Research Fund for the financial support of this work. RMC and

LDC acknowledge the University of Guelph and the Natural Sciences and Engineering Research of Council of Canada for financial support. All DFT calculations were carried out with access to supercomputing resources generously provided by Compute Canada.

References

1. Meessen, J. H. Urea. *Ullmanns Encycl. Ind. Chem.* **37**, 425–474 (2012).
2. Krausfeldt, L. E. *et al.* Urea Is Both a Carbon and Nitrogen Source for Microcystis aeruginosa: Tracking 13C incorporation at bloom pH conditions. *Front. Microbiol.* **10**, 1–12 (2019).
3. Shaw, W. H. R. & Bordeaux, J. J. The Decomposition of Urea in Aqueous Media. *J. Am. Chem. Soc.* **77**, 4729–4733 (1955).
4. Urbańczyk, E., Sowa, M. & Simka, W. Urea removal from aqueous solutions—a review. *J. Appl. Electrochem.* **46**, 1011–1029 (2016).
5. Zhu, B., Liang, Z. & Zou, R. Designing Advanced Catalysts for Energy Conversion Based on Urea Oxidation Reaction. *Small* **16**, 1–19 (2020).
6. Hu, X., Zhu, J., Li, J. & Wu, Q. Urea Electrooxidation: Current Development and Understanding of Ni-Based Catalysts. *ChemElectroChem* **7**, 3211–3228 (2020).
7. Sayed, E. T. *et al.* Direct urea fuel cells: Challenges and opportunities. *J. Power Sources* **417**, 159–175 (2019).
8. Ye, K., Wang, G., Cao, D. & Wang, G. Recent Advances in the Electro-Oxidation of Urea for Direct Urea Fuel Cell and Urea Electrolysis. *Top. Curr. Chem.* **376**, 1–38 (2018).
9. Medvedeva, X. V., Medvedev, Jury, J., Tatarchuk, S. W., Choueiri, R. M. & Anna, K. Sustainable at Both Ends: Electrochemical CO2 Utilization Paired with Electrochemical Treatment of Nitrogenous Waste. *Green Chem.* DOI: 10.1039/D0GC01754J (2020). doi:10.1039/d0gc00964d

10. Unveiling the electrooxidation of urea: the intramolecular coupling of N-N bond. *Angew. Chemie - Int. Ed.* doi:10.1002/anie.202015773

11. Zhang, L. *et al.* A Lattice-Oxygen-Involved Reaction Pathway to Boost Urea Oxidation. *Angew. Chemie* **131**, 16976–16981 (2019).

12. Vedharathinam, V. & Botte, G. G. Experimental investigation of potential oscillations during the electrocatalytic oxidation of urea on Ni catalyst in alkaline medium. *J. Phys. Chem. C* **118**, 21806–21812 (2014).

13. Forslund, R. P. *et al.* Nanostructured LaNiO3 Perovskite Electrocatalyst for Enhanced Urea Oxidation. *ACS Catal.* **6**, 5044–5051 (2016).

14. Wang, D. & Botte, G. G. In situ X-ray diffraction study of urea electrolysis on nickel catalysts. *ECS Electrochem. Lett.* **3**, 29–32 (2014).

15. Lu, F. & Botte, G. G. Understanding the Electrochemically Induced Conversion of Urea to Ammonia Using Nickel Based Catalysts. *Electrochim. Acta* **246**, 564–571 (2017).

16. Khalafallah, D., Xiaoyu, L., Zhi, M. & Hong, Z. 3D Hierarchical NiCo Layered Double Hydroxide Nanosheet Arrays Decorated with Noble Metal Nanoparticles for Enhanced Urea Electrocatalysis. *ChemElectroChem* **7**, 163–174 (2020).

17. Tesfaye, R. M., Das, G., Park, B. J., Kim, J. & Yoon, H. H. Ni-Co bimetal decorated carbon nanotube aerogel as an efficient anode catalyst in urea fuel cells. *Sci. Rep.* **9**, 1–9 (2019).

18. Xu, W., Zhang, H., Li, G. & Wu, Z. Nickel-cobalt bimetallic anode catalysts for direct urea fuel cell. *Sci. Rep.* **4**, (2014).

19. Ramesh, T. N. & Vishnu Kamath, P. The effect of 'crystallinity' and structural disorder on the electrochemical performance of substituted nickel hydroxide electrodes. *J. Solid State Electrochem.* **13**, 763–771 (2009).

20. Sun, S. *et al.* Dual tuning of composition and nanostructure of hierarchical hollow nanopolyhedra

assembled by nico-layered double hydroxide nanosheets for efficient electrocatalytic oxygen evolution. *ACS Appl. Energy Mater.* **2**, 312–319 (2019).

21. Armstrong, R. D., Briggs, G. W. D. & Charles, E. A. Some effects of the addition of cobalt to the nickel hydroxide electrode. *J. Appl. Electrochem.* **18**, 215–219 (1988).

22. Armstrong, R. D. & Charles, E. A. Some effects of cobalt hydroxide upon the electrochemical behaviour of nickel hydroxide electrodes. *J. Power Sources* **25**, 89–97 (1989).

23. Yan, X. *et al.* NiCo layered double hydroxide/hydroxide nanosheet heterostructures for highly efficient electro-oxidation of urea. *Int. J. Hydrog. Energy* **45**, 19206–19213 (2020).

24. Hao, P. *et al.* Nickel incorporated Co9S8 nanosheet arrays on carbon cloth boosting overall urea electrolysis. *Electrochim. Acta* **338**, 135883 (2020).

25. Sha, L. *et al.* The construction of self-supported thorny leaf-like nickel-cobalt bimetal phosphides as efficient bifunctional electrocatalysts for urea electrolysis. *J. Mater. Chem. A* **7**, 9078–9085 (2019).

26. He, Q. *et al.* Nickel Vacancies Boost Reconstruction in Nickel Hydroxide Electrocatalyst. *ACS Energy Lett.* **3**, 1373–1380 (2018).

27. Jiang, Y. *et al.* Simulating Powder X-ray Diffraction Patterns of Two-Dimensional Materials. *Inorg. Chem.* **57**, 15123–15132 (2018).

28. Gu, H. *et al.* Strong Catalyst-Support Interactions in Electrochemical Oxygen Evolution on Ni-Fe Layered Double Hydroxide. *ACS Energy Lett.* **5**, 3185–3194 (2020).

29. Anantharaj, S. & Kundu, S. Do the Evaluation Parameters Reflect Intrinsic Activity of Electrocatalysts in Electrochemical Water Splitting? *ACS Energy Lett.* **4**, 1260–1264 (2019).

30. Lewis, J. S., Barani, Z., Magana, A. S. & Kargar, F. The Atomic Simulation Environment — A Python library for working with atoms. *J. Phys. Condens. Matter* **29**, 0–30 (2017).

31. Kresse, G. & Furthmüller, J. Efficient iterative schemes for ab initio total-energy calculations using

a plane-wave basis set. *Phys. Rev. B - Condens. Matter Mater. Phys.* **54**, 11169–11186 (1996).

32. Kresse, G. & Furthmüller, J. Efficiency of ab-initio total energy calculations for metals and semiconductors using a plane-wave basis set. *Comput. Mater. Sci.* **6**, 15–50 (1996).

33. Wien, T. U. & Hauptstrage, W. Ab initio molecular-dynamics liquid-metal —amorphous-semiconductor simulation of the transition in germanium. *Phys. Rev. B* **49**, 251–269 (1994).

34. Physik, T., Wien, T. U. & Hauptstrasse, W. Ab. initio molecular dynamics for liquid metals. *Phys. Rev. B* **47**, 558–561 (1993).

35. A., M. J. & Vogl, P. Self-interaction-corrected density-functional formalism. I. Ground-state properties ofthe Hubbard-Peierls model. *Phys. Rev. B - Condens. Matter Mater. Phys.* **46**, 219–234 (1992).

36. Wellendorff, J. *et al.* Density functionals for surface science: Exchange-correlation model development with Bayesian error estimation. *Phys. Rev. B - Condens. Matter Mater. Phys.* **85**, 32–34 (2012).

37. Szotek, Z. & Temmerman, W. M. Application of the self-interaction correction to transition-metal oxides. *Phys. Rev. B - Condens. Matter Mater. Phys.* **47**, 4029–4032 (1993).

38. Yu, L., Ranjan, V., Lu, W., Bernholc, J. & Nardelli, M. B. Equivalence of dipole correction and Coulomb cutoff techniques in supercell calculations. *Phys. Rev. B - Condens. Matter Mater. Phys.* **77**, 1–6 (2008).

39. Wang, V., Xu, N., Liu, J. C., Tang, G. & Geng, W.-T. VASPKIT: A User-friendly Interface Facilitating High-throughput Computing and Analysis Using VASP Code. *Comput. Phys. Commun.* 1–26 (2020).

40. Momma, K. & Izumi, F. VESTA 3 for three-dimensional visualization of crystal, volumetric and morphology data. *J. Appl. Crystallogr.* **44**, 1272–1276 (2011).

41. Cococcioni, M. & De Gironcoli, S. Linear response approach to the calculation of the effective

554 interaction parameters in the LDA+U method. *Phys. Rev. B - Condens. Matter Mater. Phys.* **71**, 1–
555 16 (2005).
556 42. Calculate U for LSDA+U. *Vaspwiiki* (2019). Available at:
557 https://www.vasp.at/wiki/index.php/Calculate_U_for_LSDA%2BU. (Accessed: 20th December
558 2020)
559 43. Szytwa, A., A, M. & BALAND, A. Neutron Diffraction Study of Ni(OH)2. *Phys. Status Solidi b* **125**,
560 125–128 (1971).
561 44. Hermet, P. *et al.* Dielectric, magnetic, and phonon properties of nickel hydroxide. *Phys. Rev. B -*
562 *Condens. Matter Mater. Phys.* **84**, 1–10 (2011).
563 45. Zhang, B. *et al.* Homogeneously dispersed multimetal oxygen-evolving catalysts. *Science (80-.).*
564 **352**, 333–337 (2016).
565 46. Cui, H., Zayat, M. & Levy, D. A chemical strategy to control the shape of oxide nanoparticles. *J*
566 *Nanopart Res.* **11**, 1331–1338 (2009).
567 47. Bette, S., Dinnebier, R. E., Röder, C. & Freyer, D. A solid solution series of atacamite type
568 Ni2xMg2-2xCl(OH)3. *J. Solid State Chem.* **228**, 131–140 (2015).
569 48. Hall, D. S., Lockwood, D. J., Bock, C. & MacDougall, B. R. Nickel hydroxides and related materials:
570 A review of their structures, synthesis and properties. *Proc. R. Soc. A Math. Phys. Eng. Sci.* **471**,
571 (2015).
572 49. Poul, L., Jouini, N. & Fievet, F. Layered hydroxide metal acetates (metal = zinc, cobalt, and nickel):
573 Elaboration via hydrolysis in polyol medium and comparative study. *Chem. Mater.* **12**, 3123–3132
574 (2000).
575 50. Davidson, A., Tempere, J. F., Che, M., Roulet, H. & Dufour, G. Spectroscopic studies of nickel(II)
576 and nickel(III) species generated upon thermal treatments of nickel/ceria-supported materials. *J.*
577 *Phys. Chem.* **100**, 4919–4929 (1996).

578 51. Kimura, E., Sakonaka, A., Machida, R. & Kodama, M. Novel Nickel(II) Complexes with Doubly
579 Deprotonated Dioxopentaamine Macrocyclic Ligands for Uptake and Activation of Molecular
580 Oxygen. *J. Am. Chem. Soc.* **104**, 4257–4258 (1982).
581 52. Jayashree, R. S. & Kamath, P. V. Electrochemical synthesis of cobalt hydroxide. *J. Mater. Chem.* **9**,
582 961–963 (1999).
583 53. Khassin, A. A. *et al.* Physico-chemical study on the state of cobalt in a precipitated cobalt-
584 aluminum oxide system. *Phys. Chem. Chem. Phys.* **4**, 4236–4243 (2002).
585 54. Ma, R. *et al.* Tetrahedral Co(II) coordination in α-type cobalt hydroxide: Rietveld refinement and
586 X-ray absorption spectroscopy. *Inorg. Chem.* **45**, 3964–3969 (2006).
587 55. Frolova, Y. V. *et al.* Experimental and theoretical studies of the electronic spectra of mixed
588 framework phosphates of Zr and Co. *J. Phys. Chem. B* **108**, 6969–6980 (2004).
589 56. Nesbitt, H. W., Legrand, D. & Bancroft, G. M. Interpretation of Ni2p XPS spectra of Ni conductors
590 and Ni insulators. *Phys Chem Miner.* 357–366 (2000).
591 57. Ismail, K. M. & Badawy, W. A. Electrochemical and XPS investigations of cobalt in KOH solutions.
592 *J. Appl. Electrochem.* **30**, 1303–1311 (2000).
593 58. Zheng, X. *et al.* Theory-driven design of high-valence metal sites for water oxidation confirmed
594 using in situ soft X-ray absorption. *Nat. Chem.* **10**, 149–154 (2018).
595 59. Klaus, S., Cai, Y., Louie, M. W., Trotochaud, L. & Bell, A. T. Effects of Fe electrolyte impurities on
596 Ni(OH)2/NiOOH structure and oxygen evolution activity. *J. Phys. Chem. C* **119**, 7243–7254 (2015).
597 60. Bernard, M. C. *et al.* Structural defects and electrochemical reactivity of β-Ni(OH)2. *J. Power*
598 *Sources* **2**, 247–254 (1996).
599 61. Audemer, A., Delahaye, A., Farhi, R., Sac-Epée, N. & Tarascon, J. -M. Electrochemical and Raman
600 Studies of Beta-Type Nickel Hydroxides Ni1 − x Co x (OH) 2 Electrode Materials. *J. Electrochem.*
601 *Soc.* **144**, 2614–2620 (1997).

62. Kuznetsov, D. A. *et al.* Tuning Redox Transitions via Inductive Effect in Metal Oxides and Complexes, and Implications in Oxygen Electrocatalysis. *Joule* **2**, 225–244 (2018).

63. Huang, Z. F. *et al.* Chemical and structural origin of lattice oxygen oxidation in Co–Zn oxyhydroxide oxygen evolution electrocatalysts. *Nat. Energy* **4**, 329–338 (2019).

64. Hall, D. S., Lockwood, D. J., Poirier, S., Bock, C. & MacDougall, B. R. Applications of in situ Raman spectroscopy for identifying nickel hydroxide materials and surface layers during chemical aging. *ACS Appl. Mater. Interfaces* **6**, 3141–3149 (2014).

65. Liu, Z., Ma, R., Osada, M., Takada, K. & Sasaki, T. Selective and controlled synthesis of α- and β-cobalt hydroxides in highly developed hexagonal platelets. *J. Am. Chem. Soc.* **127**, 13869–13874 (2005).

66. Perdew, J. P., Burke, K. & Ernzerhof, M. Generalized gradient approximation made simple. *Phys. Rev. Lett.* **77**, 3865–3868 (1996).

67. Alidoust, N., Toroker, M. C., Keith, J. A. & Carter, E. A. Significant reduction in NiO band gap upon formation of Lix Ni1-xO alloys: Applications to solar energy conversion. *ChemSusChem* **7**, 195–201 (2014).

68. Wang, L., Maxisch, T. & Ceder, G. Oxidation energies of transition metal oxides within the GGA+U framework. *Phys. Rev. B - Condens. Matter Mater. Phys.* **73**, 1–6 (2006).

69. Li, Y. F. & Selloni, A. Mechanism and activity of water oxidation on selected surfaces of pure and Fe-Doped NiOx. *ACS Catal.* **4**, 1148–1153 (2014).

70. Doyle, A. D., Bajdich, M. & Vojvodic, A. Theoretical Insights to Bulk Activity Towards Oxygen Evolution in Oxyhydroxides. *Catal. Letters* **147**, 1533–1539 (2017).

71. Kalasina, S. *et al.* A new concept of charging supercapacitors based on the photovoltaic effect. *Chem. Commun.* **53**, 709–712 (2017).

72. Chen, J. & Selloni, A. First principles study of cobalt (Hydr)oxides under electrochemical

626 conditions. *J. Phys. Chem. C* **117**, 20002–20006 (2013).

627 73. Dalverny, A. L., Filhol, J. S., Lemoigno, F. & Doublet, M. L. Interplay between magnetic and orbital

628 ordering in the strongly correlated cobalt oxide: A DFT+ U study. *J. Phys. Chem. C* **114**, 21750–

629 21756 (2010).

630 74. Hunt, D. *et al.* The magnetic structure of β-cobalt hydroxide and the effect of spin-orientation.

631 *Phys. Chem. Chem. Phys.* **18**, 30407–30414 (2016).

632